Appl Phys B (2010) 101: 523–534
DOI 10.1007/s00340-010-4215-3

Applied Physics B
Lasers and Optics

Multi-terawatt laser system generating 12-fs pulses at 100 Hz repetition rate

Y. Nabekawa · A. Amani Eilanlou · Y. Furukawa · K.L. Ishikawa · H. Takahashi · K. Midorikawa

Received: 6 July 2010 / Revised version: 30 July 2010 / Published online: 17 September 2010
© The Author(s) 2010. This article is published with open access at Springerlink.com

Abstract We have developed a laser system generating high peak-power ultrashort pulses based on the chirped pulse amplification of a Ti:sapphire laser. The pulse duration of the laser is reduced to 12 fs, owing to the successful compensation of gain narrowing during amplification with novel optics. The pulse energy and the repetition rate are 40 mJ and 100 Hz, respectively, as a consequence of sufficient energy extraction from a laser medium in the final stage of a multi-pass amplifier chain, which is designed to balance focusing with a thermal lens against defocusing with convex mirrors without cryogenic cooling for Ti:sapphire crystals. The laser pulses delivered from this laser system are suitable for generating an intense attosecond pulse train in a vacuum ultraviolet or extreme ultraviolet region.

1 Introduction

The high-order harmonic (HOH) fields generated with an intense femtosecond laser pulse are now widely used for investigating ultrafast dynamics of matters. In particular, an isolated attosecond pulse (IAP) formed with the continuum spectral part of an HOH field [1–7] has revealed how fast the matter state changes under the irradiation of an intense visible laser field with a temporal resolution significantly less than 1 fs [8–11]. We recognize that two key technologies are necessary for generating the IAP. One is the stabilization of the carrier envelope phase (CEP) of an intense visible femtosecond laser pulse [12], and another is the pulse compression technique [13] using a hollow fiber, producing so-called 'a few cycle' optical pulses that form the driving laser field for HOH. Even with the distinguished achievements of IAP applications, these technologies possibly maintain IAP at a low or moderate intensity, because the pulse energy of the driving laser field is limited within a range of ∼1 mJ owing to the restriction of the intensity in a hollow core fiber and/or the difficulty of the CEP stabilization in a large-scale laser system.

On the other hand, the pulse energy of an attosecond pulse train (APT), which is formed by the Fourier synthesis of discrete HOH spectra in a plateau region [14–17], can be easily increased because we use a laser pulse with a duration of tens of femtoseconds generated from a conventional chirped pulse amplification (CPA) laser system [18] without CEP stabilization. In fact, the pulse energy and intensity of the APT or one harmonic pulse now reached more than μJ [19, 20] and 10^{12}–10^{14} W/cm^2 [21, 22], respectively, on the basis of the energy scaling criteria of HOH generation under the phase matching condition [23].

Thanks to the high intensity of an APT, we successfully observed novel phenomena of a matter interacting nonlinearly with the APT field [21, 22, 24, 25], and then we utilized these phenomena for showing directly the temporal shape of the APT in autocorrelation (AC) measurements [21, 26–30]. Nevertheless, there were two practical issues in these studies, one of which is the long data-acquisition time

Y. Nabekawa (✉) · A. Amani Eilanlou · Y. Furukawa · K. Midorikawa
Laser Technology Laboratory, Advanced Science Institute, RIKEN, 2-1 Hirosawa, Wako-shi, Saitama 351-0198, Japan
e-mail: nabekawa@riken.jp

A. Amani Eilanlou · K.L. Ishikawa · H. Takahashi
Department of Nuclear Engineering and Management, Graduate School of Engineering, The University of Tokyo, 7-3-1 Hongo, Bunkyo-ku, Tokyo 113-8656, Japan

K.L. Ishikawa
Photon Science Center, Graduate School of Engineering, The University of Tokyo, 7-3-1 Hongo, Bunkyo-ku, Tokyo 113-8656, Japan

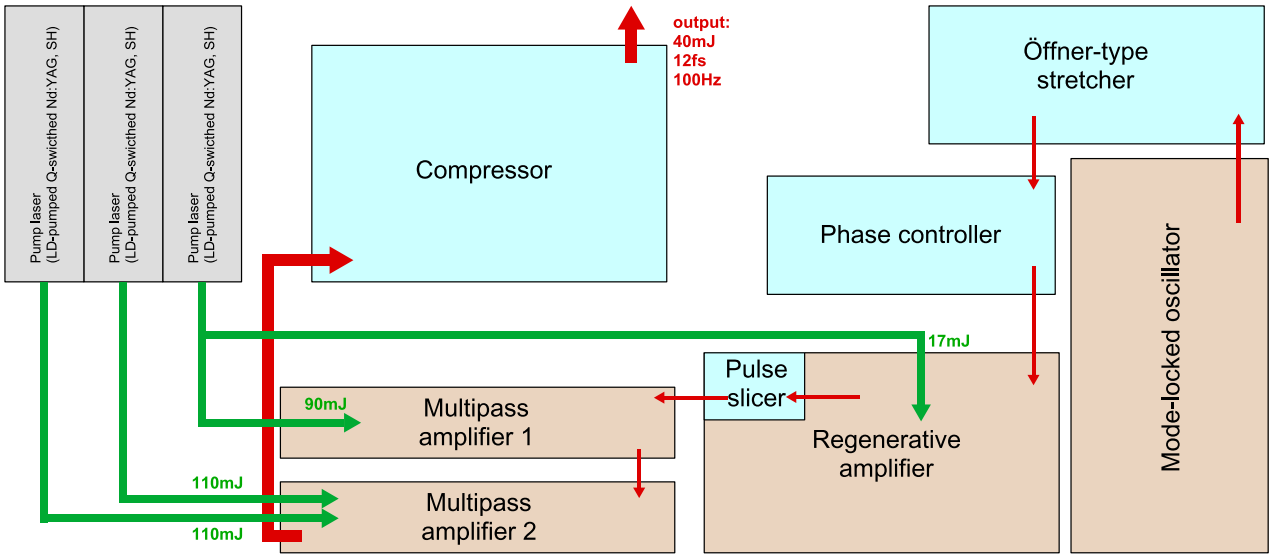

Fig. 1 Schematic diagram of laser system

required for the measurements. The repetition rate of the femtosecond laser pulse was only 10 Hz. Hence, we spent several hours or days to find appropriate AC data because the AC measurements typically require $\sim 3 \times 10^5$ shots of laser pulses. A higher repetition rate should certainly economize time for the experiment.

Another issue is the temporal shape of the APT. The train of the attosecond pulses appears 10–20 fs long in the APT [25, 31]. The duration of the train envelope was determined in Ref. [25] as the full width at half maximum of the correlation envelope by fitting the measured AC trace with the Gaussian envelope function, resulting in 15 fs. Although this APT 'envelope duration' is much shorter than the pulse duration of the driving laser field, which was 40 fs in our previous studies, it is comparable to or longer than the typical time scale of a nuclear motion in a molecule and much longer than the time period of an electron motion in an atom. The reduction in APT envelope duration into a few fs regime would make it possible to resolve, at least, the vibrational motion of the second lightest homonuclear molecule, deuterated hydrogen [11], even though the attosecond dynamics of an electron motion might still be buried in the APT envelope.

In this paper, we report on the CPA system of a Ti:sapphire laser developed to generate intense APT fields that can be more conveniently applied to explore the ultrafast dynamics of atoms and molecules on a sub-10-fs time scale. We have increased the repetition rate of the laser pulse to 100 Hz, which is tenfold higher than that of a laser pulse used in previous APT experiments, while maintaining a similar pulse energy at 40 mJ. We have also shortened the pulse duration down to 12 fs, so that we can expect the 'train envelope' duration of the APT generated from this laser pulse to be much shorter than 10 fs.

We know that a scheme of optical parametric chirped pulse amplification (OPCPA) [32] has the advantage of broad gain bandwidth for a multi-TW laser system [33, 34]. The most crucial issue in the OPCPA laser system is the development of pumping laser sources, with a pulse duration of several tens of picoseconds, which have to be exactly synchronized with the amplified laser pulse and have a sufficiently good beam quality in the spatial profile. In contrast, high-energy Q-switched Nd:YAG lasers with 100 Hz repetition rate as pumping laser sources of Ti:sapphire laser are now commercially available. This is the reason why we have decided to develop a "classic" CPA laser system instead of an OPCPA laser system.

In the next two sections, we describe the details of the laser system and then briefly introduce the prospects for its application.

2 Laser system description

2.1 Overview

We show a schematic figure of the laser system in Fig. 1. The system is organized in accordance with a typical CPA scheme. A seed pulse, generated from a mode-locked oscillator, is stretched in an Öffner-type stretcher [35], then amplified in an amplifier chain consisting of a regenerative amplifier and two cascaded multipass amplifiers. We use three LD-pumped Q-switched Nd:YAG lasers as pumping laser sources for this amplifier chain. The pulse energy of the second-harmonic (SH) pulse of each Q-switched laser is 120 mJ at maximum. After passing through a grating pair compressor, the pulse duration of the amplified

pulse is shortened to 12 fs. A phase controller with a liquid crystal light modulator (LC-SLM) [36, 37] located behind the stretcher compensates for the spectral phase distortion caused by material dispersions in the laser system. A pulse slicer, in which a Pockels cell is placed between two polarizers with a crossed polarization geometry, isolates the regenerative amplifier from the cascaded multipass amplifiers.

The main features of this laser system are (i) the relatively high average power due to the moderate repetition rate (100 Hz) and high pulse energy of each pumping laser (∼100 mJ) and (ii) the broad spectral width that can support a sub-15 fs pulse. The former feature requires the compensation for a thermal lens effect in a laser crystal. The latter cannot be achieved without considering the gain narrowing effect during amplification. Thus, we explain the system design for these features, followed by the description of the experimental results in each part of the laser system, in this section.

2.2 Thermal management

It is well known that a thermally induced lens effect in a solid state laser crystal significantly affects the spatial quality of the amplified laser beam and energy extraction efficiency from the pumping laser. This is mainly due to the refractive index change of the laser crystal with the temperature gradient, resulting in the thermal focusing power, defined as a reciprocal of the focal length of the thermal lens f_{th}, to be shown as [38]

$$f_{\mathrm{th}}^{-1} = g(dn/dT)(F\nu_{\mathrm{rep}}/K_{\mathrm{th}}), \tag{1}$$

where dn/dT, K_{th}, and g are the refractive index change per unit temperature, the thermal conductivity of the laser crystal, and a constant defined by a model of the thermal lens effect, respectively. We also notate the pumping fluence as F and the repetition rate of the laser pulse as ν_{rep} in this equation.

Currently, many of the commercially available CPA systems of high-average-power Ti:sapphire lasers adopt cryogenic cooling units for Ti:sapphire crystals to lower the temperature [39] because the factor $dn/dT \cdot K_{\mathrm{th}}^{-1}$ under the boiling temperature of liquid nitrogen is approximately 100-fold lower than that at room temperature. Thus, the thermal focusing power in the Ti:sapphire crystal should be crucially low such that we can neglect the wavefront correction of the amplified beam behind the Ti:sapphire crystal in the design of a multipass amplifier.

In spite of the advantage of cryogenic cooling, we have cooled all Ti:sapphire crystals in the laser system with only circulating water at a temperature of 14∼15°C for simplicity. There is no vacuum chamber, input and output windows, vacuum pump, pressure gauge, and even temperature gauge in the amplifiers. We have, instead, carefully evaluated the thermal lens effect and the robustness of the amplifier design against the change in pumping fluence. This kind of thermal lens analysis was demonstrated by Salin et al. [40]. They treated a bow-tie multipass amplifier containing a Ti:sapphire crystal and folding mirrors as a quasi-cavity with a convex lens and two flat end mirrors to find the stability condition of the quasi-cavity. Nabekawa and coworkers employed this method with modifications of the quasi-cavity, consequently, achieving TW-class laser systems with 1 kHz [41] and 5 kHz repetition rates [42].

As for the thermal lens effect under similar repetition rate and pumping fluence in the laser system described in this paper, Ito et al. measured the focal length, f_{th}, which depends on the pumping power density, to be 5.7 m at a fluence of 2.14 J/cm^2 at 50 Hz repetition rate [43]. They have successfully compensated for this thermal lens effect with a spherical convex mirror in a triangular configuration of a multipass amplifier, and then, obtained 24-fs pulses at a peak power of 7 TW [44].

We have designed a kind of bow-tie multipass amplifier containing two convex mirrors to counterbalance focusing with the thermal lens, based on this measured f_{th}, as shown in schematics in Figs. 2(a) and (b). In these two models of the quasi-cavity for the multipass amplifier, the thermal focusing power is assumed to be in a range that is approximately five times higher than the measured f_{th} by Ito and coworkers, because the repetition rate is twofold (100 Hz) and the pumping fluence should be more than twice those under the measuring conditions. The high pumping fluence is required to obtain a sufficient gain in very short (∼720 nm) and long (∼900 nm) wavelength regions with small emission crosssections of the Ti:sapphire laser. To balance such a tight focusing effect, we have used two convex mirrors in the quasi-cavity, resulting in a stable condition. Detailed parameters used for these calculations are shown in Table 1. We determined the pump energy and heat dissipation in this table in accordance with the experimental conditions for the first (a) and second (b) multipass amplifiers. The radius of curvature of the convex mirror and the cavity configuration were, then, adjusted such that the beam radius at the Ti sapphire crystal was similar to that of the pumping beam at a fixed fluence of 9 J/cm^2 (5.2 J/cm^2) for the calculation of red solid and brown dotted curves in Figs. 2(a), (b). We assume the spatial profile of the pumping beam to be circular and top-hat-shaped. Hence, the beam radius of the pumping beam is just $\sqrt{E/(\pi F)}$, where E is the pumping energy, while the radius of the amplified beam is defined as the e^{-2} half width with the assumption of the Gaussian beam profile. Note that the pumping fluence in the Brewster cut rod of the Ti:sapphire crystal, which is used in the cavity depicted in Fig. 2(a), is reduced by a factor of refractive index (≃1.76).

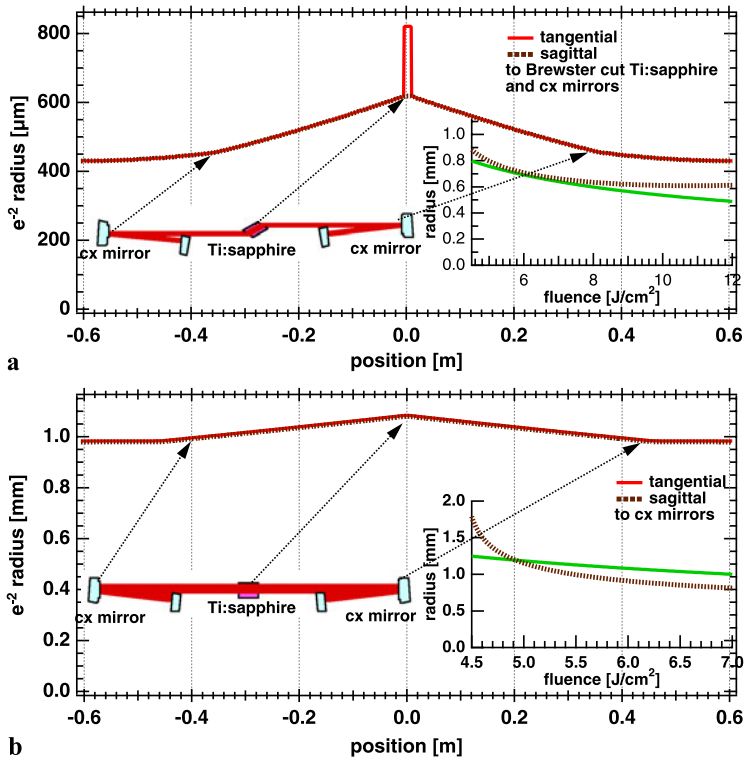

Fig. 2 Evolution of beam radius (e^{-2} half width) in quasi-cavity model of multipass amplifier. We have adjusted the radii of the two convex mirrors and cavity length such that the beam radius in the Ti:sapphire rod is suitable for the first multipass amplifier in (**a**) and for the second multipass amplifier in (**b**). Resulting cavity parameters are summarized in Table 1. The *red solid* (*brown dotted*) curve corresponds to the beam radius on the tangential (sagittal) plane defined by the incident and reflection beams for the convex mirrors. We also show, as a *dotted brown curve*, the alteration of the beam radius at the center of the Ti:sapphire rod on the sagittal plane against the change in pumping fluence, in the *inset* of each figure. The *solid green curve* indicates the beam radius of the pumping beam. Note that the pumping fluence shown in the *inset* in (**a**) is reduced in the Brewster cut rod of the Ti:sapphire crystal by a factor of refractive index

The evolution of the beam radius on the tangential plane, depicted as a red solid curve, is almost the same as that on the sagittal plane, shown as a brown dotted curve, in both Figs. 2(a) and (b). Thus, we can expect a circular beam profile of the laser pulse from these modeled amplifiers.

It is often the case that the pumping fluence should be adapted by changing the beam radius so as to operate the amplifier correctly under the actual experimental conditions with the inaccuracy of the titanium dopant in the Ti:sapphire crystal, the spatial inhomogeneity of the pumping beam, and many other issues that are not considered in the calculation model mentioned above. Therefore, it is worth to simulate the performance of this amplifier against the change in pumping fluence. The insets in Figs. 2(a) and (b) show the alteration of the e^{-2} half width of the amplified beam at the center of the Ti:sapphire crystal (dotted brown curve) and the radius of the pumping beam (solid green curve) due to the change in pumping fluence. Although the e^{-2} half width of the amplified beam rapidly increases with the decrease in pumping fluence in the inset of Fig. 2(b), the beam radii of the pumping and amplified beams are similar in the region from 6 to 12 J/cm^2 for the first multipass amplifier and in the region from 5 to 7 J/cm^2 for the second multipass amplifier. This spatial mode matching behavior of the amplifier insures its robustness against the inaccuracy of the pumping fluence under the realistic conditions.

We have adopted the configuration of the multipass amplifiers listed in Table 1 as a consequence of the analysis of these quasi-cavities.

Table 1 Cavity parameters used for calculation of beam radius shown in Fig. 2. R: radius of curvature of convex mirror, $L1$: separation between convex mirror and Ti:sapphire crystal, $L2$: separation between convex mirror and end mirror, η: dissipation from pump energy to heat

	(a)	(b)
R	−5 m	−10 m
$L1$	0.35 m	0.4 m
$L2$	0.25 m	0.15 m
Ti:sapphire	Brewster cut, 12 mm long	Normal cut, 12 mm long
pump energy	90 mJ	220 mJ
η	77%	45%

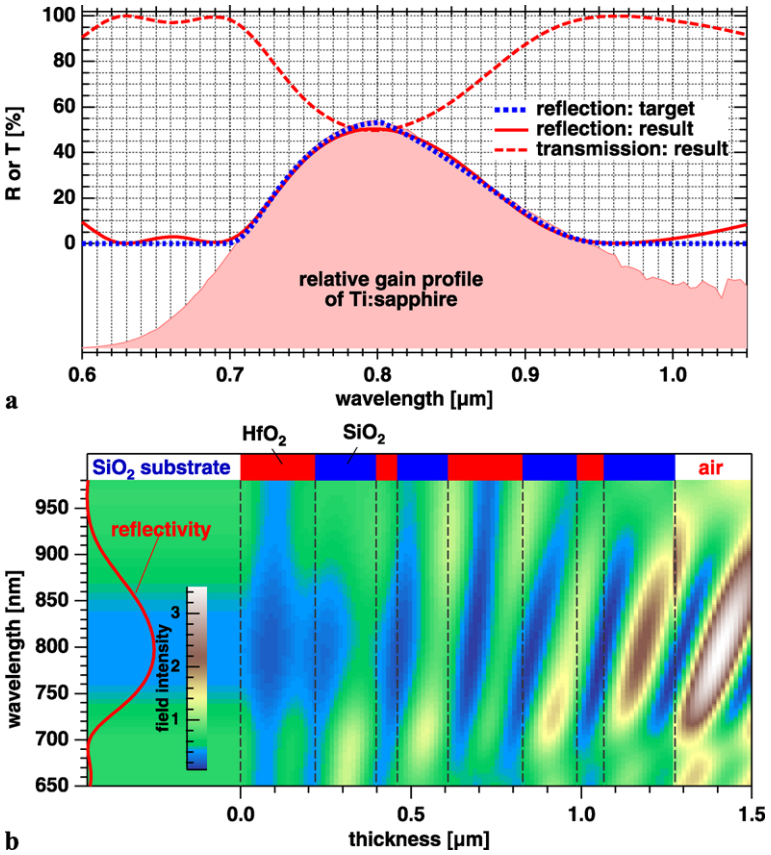

Fig. 3 Example of GNC design (code number type Y2). We assume HfO_2 and SiO_2 films to be high- and low-index film materials, respectively. (**a**) Gain profile of Ti:sapphire laser (*red hatched area*) and fitted curve (*blue dotted curve*) as target reflectivity profile for film-design optimization. The resultant reflectivity (*red solid curve*) and transmission (*red dashed curve*) are also shown. (**b**) The positions and thicknesses of film materials are shown above the field intensity image. We put a semi-infinite SiO_2 substrate at the position less than 0 μm in the calculation. The reflectivity of the GNC is depicted as a *red solid curve*

2.3 Gain narrowing compensation

The most crucial issue for shortening the pulse duration of the amplified pulse generated from the CPA laser system is how we can effectively keep the broad spectrum of the pulse during amplification. The spectrum of the amplified pulse, in general, tends to become narrower because of the dependence of the gain profile on wavelength (gain narrowing effect). Fortunately, we have the experience of developing a sub-10-fs CPA laser system at 10 Hz repetition rate [45]. The gain narrowing effect was properly relaxed in this laser system by inserting a special optics called the 'gain narrowing compensator (GNC)' in regenerative and multipass amplifiers. The GNC is a kind of partial mirror, which is designed for mostly reflecting the spectral component near the peak gain of the Ti:sapphire laser and transmitting the other spectral components.

The idea of inserting a wavelength-dependent loss in a regenerative amplifier to compensate for gain narrowing was proposed and demonstrated by Barty et al. more than 10 years ago [46]. Since then, there have been many attempts to control the amplified spectrum in a CPA laser system [46–50]. Our GNC is classified as a partial mirror of the dielectric film coating developed by Takada et al. [51, 52]. Nevertheless, it is quite different from the partial mirror with typical quarter-wave stacked films indicated in Refs. [51, 52] because the constitution of the films is optimized by using an iterative algorithm such that the reflectivity should be matched with the gain profile of the Ti:sapphire laser.

We show the calculated reflectivity (R) and transmission ($T = 1 - R$) of the GNC type Y2, used in the sub-10-fs CPA laser system described in Ref. [45], as solid and dashed red curves in Fig. 3(a), respectively. To obtain the reflectivity profile of this GNC, we, first, fitted the gain profile of the Ti:sapphire laser [53], $g(\lambda)$, shown as a hatched area in Fig. 3(a) to the analytical function of $\{f(x)\}^{\alpha}$ in the wavelength range needed for amplification (700–950 nm), and then, the thicknesses of the stacked films are iteratively optimized by using the dumped least-squares method (DLSM) [54] so as to minimize the cost function between the reflectivity profile and the fitted gain profile as a target.

We note that we define λ as the wavelength, and x is a normalized wavelength with a fitting parameter λ_0. The function $f(x)$ is expressed as $f(x) \equiv \exp\{-1/(1 - x^{2n}) + 1\}$ for $|x| < 1$ and $f(x) = 0$ for $|x| \geq 1$. The other fitting parameters in the fitting functions are α, integer n, and an amplitude not shown explicitly. We can reproduce the asymmetry of the gain profile by switching the fitting parameters in a wavelength region shorter than 800 nm to those in a wavelength region longer than 800 nm. The fitting function $f(x)$

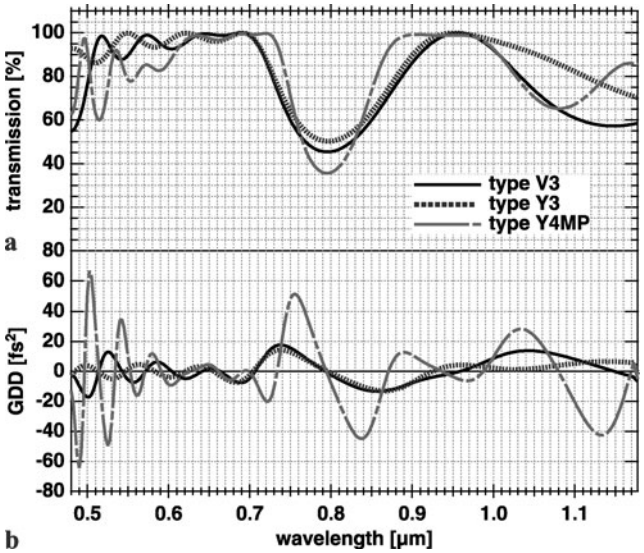

Fig. 4 Three kinds of GNC designs: (**a**) transmission, (**b**) GDD of transmitted light, which are used in 100-Hz 12-fs laser system

is useful for smoothly connecting the reflectivity curve in the range of 700–950 nm to the 0 reflectivity line in the other wavelength range, because it has finite support and is infinitely differentiable.

We cannot change the number of films during the iteration of DLSM. We need trial and error to determine the number of films appropriately. The resultant number of layers is so small that the group-delay dispersion (GDD) for the transmitted laser pulse can be removed with the LC-SLM phase controller; therefore, we do not give the DLSM the constraint for the GDD. The incident angle is fixed at the Brewster angle of the SiO_2 substrate in order to suppress the Fresnel loss on another surface of the substrate without using an antireflection coating. We assume the incident light to be p-polarized. An example (GNC type Y2) of dielectric film layers that exhibits the reflectivity profile in Fig. 3(a) is shown in blue and red above Fig. 3(b). The intensity distribution of light electric field in these layers is also depicted with a false color image. There are eight layers in the coating with HfO_2 and SiO_2 films, and these layers have different thicknesses. We can expect the damage threshold of this coating to be comparable to the high-damage-threshold (HDT) mirror because the maximum intensity in the film layers is similar to that in the HDT mirror coating mentioned later.

We varied the target reflectivity profile by adding the exponent β to the gain profile, $\{g(\lambda)\}^{\beta}$, and changing the relevant spectral range for the fitting procedure. We designed and fabricated more than ten kinds of GNC from various target reflectivity profiles. We have chosen three kinds of GNC, namely, type V3, type Y3, and type Y4MP, after some experimental trials. The transmission and GDD profiles of each GNC are shown in Figs. 4(a) and (b), respectively.

The first two GNCs are suitable for simultaneous insertion in the cavity of the regenerative amplifier. The broad spectral width of transmission loss is advantageous for the regenerative amplifier, in which the amplified pulse passes through the GNCs and Ti:sapphire crystal many times under a relatively low gain condition. The third GNC should be placed in one of the passes of a multipass amplifier, in which the single-pass gain is much higher than that of the regenerative amplifier. The narrow and deep dip of the transmission profile is adopted for this condition.

2.4 Mirror coating

Dielectric coatings on many reflective optics used in the laser system may restricts the spectral bandwidths of amplified pulses. A chirped mirror coating fabricated with high-damage-threshold (HDT) dielectric film materials [55] has the advantage of broad bandwidth for the reflectivity. In the 100-Hz CPA laser system described in this paper, however, we do not use HDT chirped mirrors. The main drawback of the HDT chirped mirrors was the oscillation of GDD that cannot be removed without using an active dispersion controller, such as an LC-SLM. We have employed a hybrid dielectric film coating, proposed by Takada et al. [56], for high-reflection mirrors used in the laser system, instead of the HDT chirped mirror coating, to avoid the complexity for the correction of the GDD oscillation. The spectral width of the hybrid dielectric film coating is sufficiently broad to support the spectral component of a 12-fs pulse, although it is narrower than that of the HDT chirped mirror coating.

We show the design of reflectivity and GDD for the hybrid dielectric film coating as solid curves in Figs. 5(a) and (b), respectively. The coating consists of eleven pairs of TiO_2/SiO_2 films with an optical thickness of 200 nm cover-coated with seven pairs of HfO_2/SiO_2 films with the same optical thickness. The broadband reflectivity should be obtained using the high reflective index of the TiO_2 films, whereas we can prevent these low-damage-threshold films from breaking by reducing the laser field intensity with the HDT mirror coating of HfO_2/SiO_2 film layers. We can see in Fig. 5(a) that the spectral width for the reflectivity of the hybrid coating exhibits a middle range property between that of the broadband coating with TiO_2/SiO_2 film layers and that of the HDT coating with HfO_2/SiO_2 film layers, as we have expected. Although the GDD profile of the hybrid coating in Fig. 5(b) is more similar to that of the HDT coating rather than that of the broadband coating, it is limited at ± 80 fs^2 in the wavelength range from 720 nm to 900 nm. We can easily eliminate the dispersion due to multiple reflections with this coating with an LC-SLM phase controller.

The simulated result of the optical field intensity distribution in the films of the hybrid coating is also shown in Fig. 6. The maximum field intensity in TiO_2 film layers is

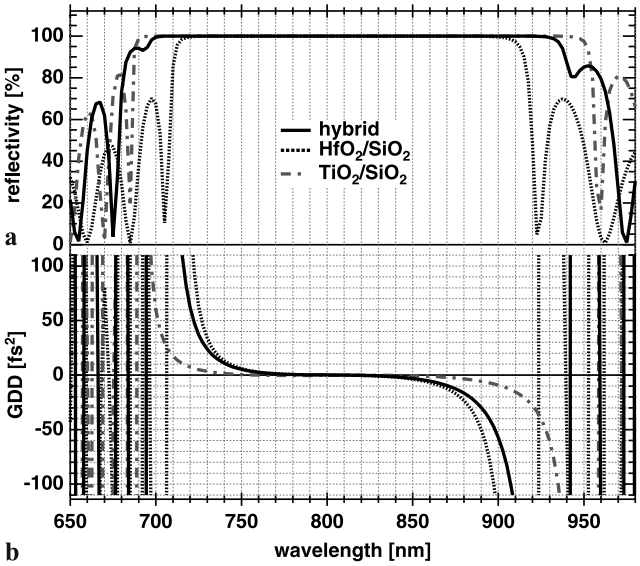

Fig. 5 Design of mirror coatings. (**a**) Reflectivity. (**b**) GDD. The *solid curve* in each figure shows the calculated result of the hybrid mirror coating using both TiO_2/SiO_2 and HfO_2/SiO_2 film pairs. We also show the conventional broadband mirror design, made of eighteen pairs of TiO_2/SiO_2 films, as *dash-dotted curves*, and HDT mirror design, made of eighteen pairs of HfO_2/SiO_2 films, as *dotted curves*

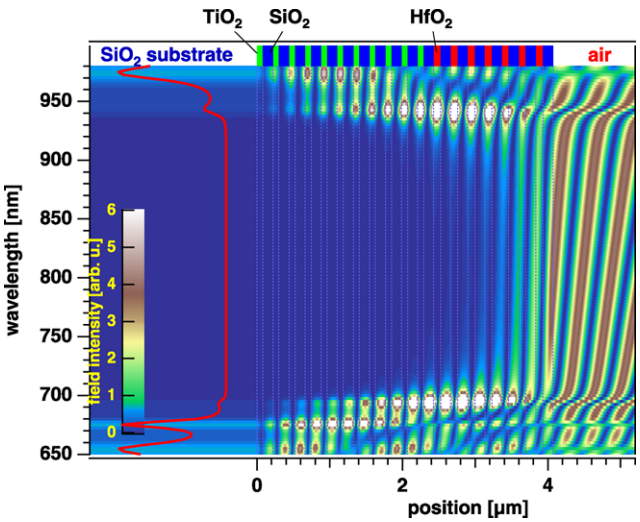

Fig. 6 Field intensity distribution in dielectric film layers of hybrid film coating depending on wavelength. The light electric field comes from the right-hand side and is reflected in the same direction. The positions and thicknesses of film materials are shown above the field intensity image. We put a semi-infinite SiO_2 substrate at the position less than 0 μm in the calculation. The reflectivity of the hybrid coating is depicted as a *red solid curve*

reduced to less than 1/20 that in HfO_2 film layers in the wavelength range from 720 nm to 900 nm. Therefore, the weak TiO_2 film layer is secure from the penetration of a strong Ti:sapphire laser field.

We have adopted this design of the hybrid coating for the cavity mirrors of a regenerative amplifier and the spherical

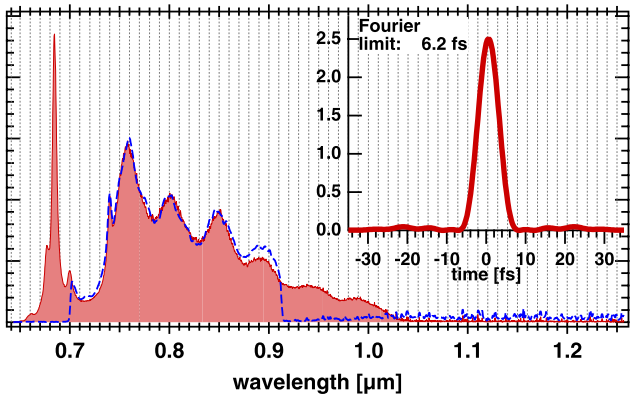

Fig. 7 Spectrum of mode-locked laser pulse generated from oscillator (*red hatched area*). The temporal profile calculated from the spectrum under the Fourier limit condition is shown in the *inset*. The spectrum behind the LC-SLM phase controller is also shown as a *blue dashed curve*

concave and convex mirrors used for telescopes to adjust the beam radius of the amplified pulse. The coating design of folding mirrors at 45° incidence is the same as that used in the sub-10-fs CPA laser system.

2.5 Front-end for the amplifiers

The seed pulse of the laser system is generated from a home-built mode-locked oscillator with a Z-fold cavity consisting of a pair of concave mirrors with a radius of curvature of 50 mm, folding mirrors and an output coupler. A pair of thin wedge plates made of silica is also put in the cavity with a Brewster incident angle to the intracavity laser beam. The positive dispersion in the cavity, which mainly originates from a 3-mm-thick Ti:sapphire crystal and the pair of wedge plates, is canceled out with two pairs of chirped mirrors (LAYERTECH). The net dispersion is finely tuned by adjusting the insertion of one of the wedge plates so that the spectral width of the mode-locked laser pulse is maximized. We show the spectrum of the mode-locked laser pulse from the oscillator in Fig. 7. The spectrum spans from 650 nm to 1030 nm and the shortest pulse duration expected from this spectrum under the Fourier limit condition is 6.2 fs, as shown in the inset of this figure. The output power of the oscillator is 110 mW at a pumping power of 1.6 W.

The seed pulse is collimated with a telescope and then sent to an Öffner-type stretcher [35] consisting of a convex mirror with a radius of curvature of −300 mm, a concave mirror with a radius of curvature of 600 mm, a grating with a groove density of 1200 g/mm, and folding mirrors. The incident angle of the laser pulse to the grating is 41.2°. The grating position from the common center of the curvatures of the two spherical mirrors is set to ∼230 mm. Thus, the GDD of the stretcher is estimated to be ∼1.3 ps^2 and the group-delay difference between the spectral components at 720 nm

and 900 nm, which respectively correspond to the shortest and longest spectral edges of an amplified pulse, is more than 600 ps. This large group delay ensures to prevent hazardous nonlinear effect (self-focusing) in Ti:sapphire crystals, which must be strongly pumped to obtain a sufficient gain in the wavelength region of a low-emission cross section, at the next stage of an amplifier chain.

The stretcher is followed by an LC-SLM (JENOPTIK SLM-S640) phase controller [36]. In this phase controller, we put a sequence of three Brewster cut prisms made of SF57 glass to provide angular dispersion at the focal point of a concave mirror with a radius of curvature of 1200 mm. After collimation with the concave mirror, the spectrally dispersed laser pulse is reflected back with a flat mirror placed at another focal point of the concave mirror, and the pulse goes through again the sequence of prisms with the compensation of spectral dispersion, and then finally, the pulse is picked off with a folding mirror. The LC-SLM is inserted immediately in front of the flat mirror, resulting in a double-pass configuration of the LC-SLM in the 4f-confocal geometry of the concave mirror. Of the 640 channels of the LC-SLM, 440 channels are allocated in the spectral range from 720 nm to 900 nm. The spectral or frequency resolution in each channel of the LC-SLM changes according to the wavelength because of the nonlinearity of the angular dispersion of the prism sequence. Typical spectral (frequency) resolutions at the wavelengths of 720 nm, 800 nm, and 900 nm are 0.26 nm/ch, 0.41 nm/ch, and 0.65 nm/ch (0.15 THz/ch, 0.19 THz/ch, and 0.24 THz/ch), respectively. The modulation amplitude of the phase can be more than 20 rad, which is larger than that of the phase distortion in the laser system estimated by a ray-trace analysis. The spectrum of the pulse behind the LC-SLM is shown as a blue dashed curve in Fig. 7. Spectral clippings at both sides are attributed to the restriction of the sizes of the concave and convex mirrors used in the stretcher.

2.6 Amplifier chain

The output pulse from the LC-SLM phase controller is sent to an amplifier chain consisting of a regenerative amplifier and a sequence of four-pass and three-pass amplifiers. We put a telescope in front of each amplifier for spatial mode matching. A pulse slicer with a Pockels cell and two crossed polarizers excludes the spontaneous emission coming from the regenerative amplifier from being amplified in the first multipass (four-pass) amplifier.

The regenerative amplifier contains two concave mirrors with radii of curvatures of 750 mm and 500 mm, and two other flat end mirrors, resulting in an X-fold cavity. We also inserted a pair of prisms (s-LAH64, Ohara) in one arm of the X-fold cavity to relax the condition of compensation for high-order dispersion. We installed a Pockels cell and a thin film polarizer in another arm of the X-fold cavity for the injection and rejection of the pulses. A Ti:sapphire crystal is placed near the confocal position of the two concave mirrors. The GNC type V3 and type Y3 are both located between the end mirror and one of the prisms. We can control the spectrum of the amplified pulses by adjusting the incident angles of these GNCs to the intracavity laser beam.

The laser delivering the pumping pulse to the regenerative amplifier is an LD-pumped Q-switched YAG (Thales, JEDI) with a repetition rate of 100 Hz and a pulse duration of 9 ns. The SH output from this laser is split into two beams with a partial mirror, one of which is used for operating the regenerative amplifier. The other beam is sent to the first multipass amplifier.

After 16 round trips in the cavity of the regenerative amplifier, the pulse is rejected and send to the pulse slicer. The pulse energy of the amplified pulse, measured behind the pulse slicer, is 70 μJ, which is crucially lower than the pumping pulse energy of 17 mJ. This low efficiency of the regenerative amplifier is consistent with the previous experimental result in the sub-10-fs amplifier [45], and thus, is inevitable owing to great losses on the repeated reflections on the GNCs during round trips of the amplified pulses in the cavity. The amplified spontaneous emission (ASE) contained in the amplified pulse is estimated to be less than 6% from the measured pulse shape in the nanosecond range with a fast PIN photodiode.

In the next two stages of the multipass amplifier, the spatial quality of the pumping laser beam is important because the cross section of the pump pulse should be increased so that the fluence of the amplified pulse saturates after high-energy amplification. The spatial profile of the pumping laser measured just behind the exit of the laser head is shown in Fig. 8(a). We can observe a narrow central area confined at ± 1 mm and a broad pedestal area spanning to ± 3 mm in both the horizontal and vertical directions. Such a peaky profile is disadvantageous for pumping a Ti:sapphire crystal because the peak fluence of the pumping beam may exceed the damage threshold of the crystal when we adjust the fluence at the pedestal to be sufficiently high for amplification. Therefore, we have searched for the position, along the propagation axis of the beam, where the peaky spatial profile is more relaxed, and then, found that the spatial image in the amplifier rod of the pumping laser is very suitable. We have transferred this spatial image with a telescope and a relay lens with an appropriate magnification factor for each multipass amplifier.

The resultant spatial profile at the equivalent position of the Ti:sapphire crystal in the second multipass amplifier is shown in Fig. 8(b). A top-hat beam in this figure is ideal for the coaxial pumping of the Ti:sapphire crystal. Furthermore, there are no ring-shaped fringes, which usually appear in the beam generated from a high-energy Q-switched YAG laser

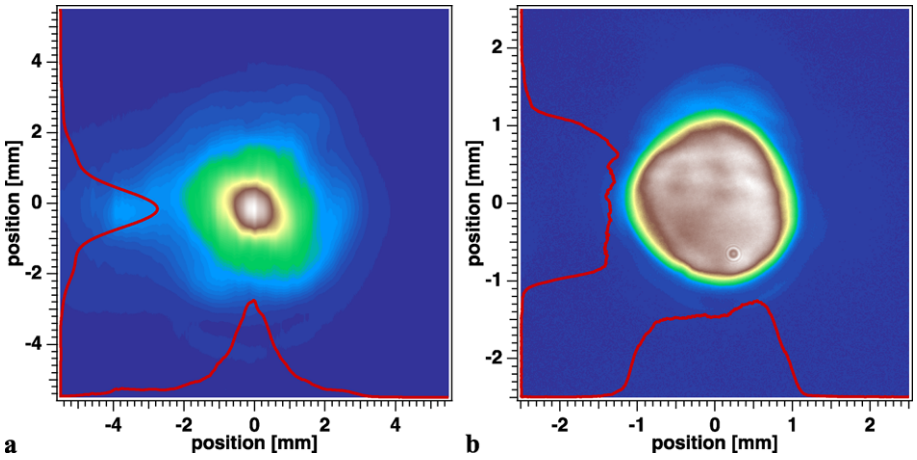

Fig. 8 Spatial profiles the pumping laser measured just behind laser head (**a**) and at equivalent position of Ti:sapphire crystal in second multipass amplifier (**b**). The area profiles along the horizontal and vertical directions are depicted as *red curves* in each figure

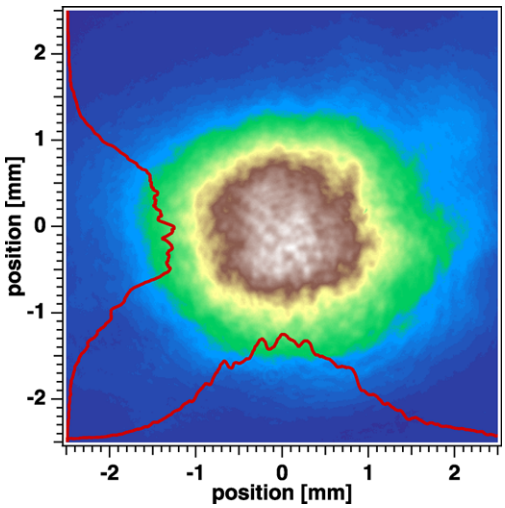

Fig. 9 Spatial beam profile of Ti:sapphire laser pulse from first multipass amplifier. The area profiles along the horizontal and vertical directions are also shown as *red solid curves*

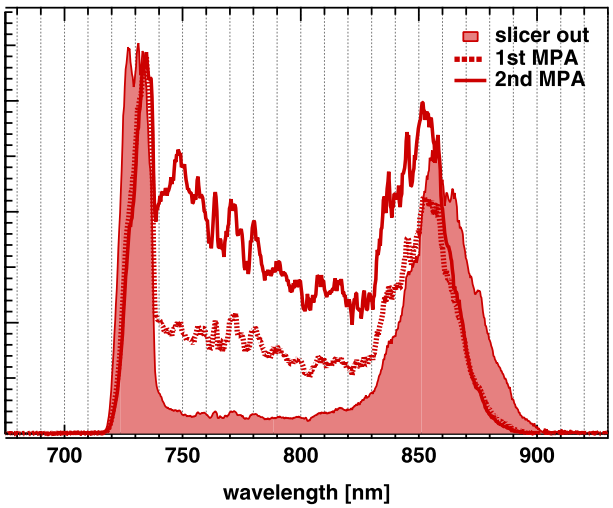

Fig. 10 Spectra, behind pulse slicer (*red hatched area*), behind first multipass amplifier (*red dotted curve*), and behind second multipass amplifier (*red solid curve*)

with a Gaussian coupler. We can also see that the beam diameter is similar to that of the design depicted in the inset of Fig. 2(b); hence, we have expected an efficient energy extraction from the multipass amplifier stages.

In fact, the output energies from the first four-pass and second three-pass amplifiers are 12 mJ and 90 mJ, with pumping energies of 90 mJ and 220 mJ, respectively. The energy extraction efficiency against the absorbed pumping energy (92% of the pumping energy) of the first amplifier is 14%, which is relatively low compared with that of a conventional multipass amplifier. This is due to the loss of the GNC type Y4MP placed between the first and second passes in the amplifier. The extracted pulse energy from the second amplifier is 38% of the absorbed pump pulse energy, which is reasonably high in the TW-class high-repetition-rate Ti:sapphire laser system.

The spatial profile of the amplified pulse from the first multipass amplifier is nearly Gaussian shaped, as shown in Fig. 9, with some weak outer rings that emerge out of the detection area of a CCD camera. The profile was measured at the equivalent position of the Ti:sapphire crystal in the second multipass amplifier before installing the second multipass amplifier. This result ensures the feasibility of the design of the quasi-cavity for the high-energy multipass amplifier at 100 Hz repetition rate. The output pulse from the second multipass amplifier is also nearly Gaussian shaped, whereas the intensity of the outer part is high. This may be owing to the fact that the thermal lensing power in the actual amplifier is lower than that we expected in the quasi-cavity model. The beam radius of the amplified pulse under this condition should be relatively larger than that of the pump beam; hence, the spatial part outside of the pump beam does not couple with the quasi-cavity mode.

We show the change in the spectral shape for each amplifier stage in Fig. 10. The deep and wide spectral dip ranging from ∼740 nm to ∼830 nm appearing in the spectrum of the

pulse behind the pulse slicer (the spectrum of the pulse amplified with the regenerative amplifier), is gradually buried with the progress of amplifier stages. Spectral width is reduced during the amplification in the first multipass amplifier owing to the gain narrowing accompanied by a high amplification factor of 170 (≃12 mJ/70 μJ). Nevertheless, the spectrum of the pulse generated from the second multipass amplifier still exhibits a sufficient spectral width necessary for forming a pulse of less than 12 fs as the Fourier limit.

2.7 Pulse compression

The amplified pulse from the second multipass amplifier goes through a Glan-laser prism polarizer, subsequently improving the extinction ratio of the harmonic separator mirrors [57] used for HOH.

After the magnification of the beam with a telescope, the amplified pulse is sent to a pulse compressor consisting of a pair of gratings with a groove density of 1200 g/mm and roof mirrors. The incident angle to and separation between the gratings were adjusted so as to shorten the pulse duration as much as possible. Then, we measured the spectral phase of the pulse behind the compressor by spectral interferometry for direct electric-field reconstruction [58]. The result is shown as a gray dotted curve in Fig. 11(a). We did not expect a large phase modulation at ∼397 THz in the measured phase from our ray-trace analysis of the dispersion in the entire laser system. We have not yet determined the reason for such phase modulation so far. We suspect that the distortions of the spherical mirrors in the stretcher cause the phase error [59].

The phase modulation, however, could be removed by using the LC-SLM phase controller set between the stretcher and the regenerative amplifier. We have fed back the inverse of the measured spectral phase to the phase controller twice and then obtained the spectral phase shown as a black solid curve in Fig. 11(a). We can coarsely see the spectral phase as a flat line. The amplitude of the fine modulation in the phase is estimated to be 0.35 rad as the root-mean-square error in the frequency range from 341 THz to 414 THz. We can reconstruct the temporal profile of the compressed pulse from the measured phase (black solid curve in Fig. 11(a)) and spectrum (red hatched area in Fig. 11(a)), as shown in Fig. 11(b). We observe many pedestals in front of the main peak of the pulse, which are much more than those of the Fourier limit pulse depicted as a dotted curve in this figure, owing to the imperfect removal of the phase error. Nevertheless, the pulse duration is sufficiently short to almost reach the Fourier limit, resulting in 11.8 fs.

Before introducing the pulse to the compressor, the pulse energy is reduced from 90 mJ to 71 mJ during the reflections of steering mirrors behind the magnification telescope. This energy loss is caused by the spatial clipping of the outer

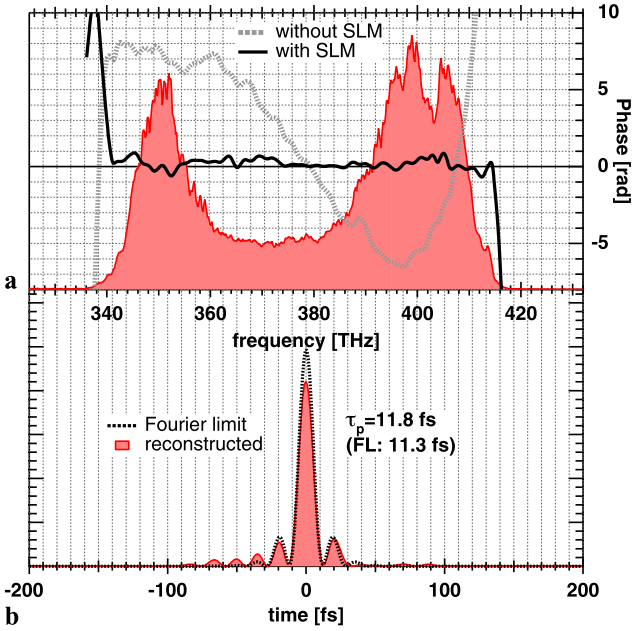

Fig. 11 (**a**) Spectrum behind compressor (*red hatched area*) and measured spectral phase without (*gray dotted curve*) and with (*black solid curve*) LC-SLM phase controller. (**b**) Temporal profile of pulse calculated from measured spectrum and spectral phase (*red hatched area*). The Fourier limit pulse is also shown as a *black dashed curve*

part of the amplified beam with the restriction of the size (2″ diameter) of the steering mirrors at 45° incidence. The pulse energy behind the compressor is 40 mJ. Therefore, the throughput of the compressor is estimated to be 56%. A simple calculation dividing the pulse energy by the pulse duration leads a peak power of the laser pulse (40 mJ/12 fs) to more than 3 TW, although we have to evaluate the energies contained in the pedestals and the ASE to determine the peak power correctly. We will measure the pulse contrast on a time scale of fs or ps if we need to determine the effects of precursors against the main pulse in the HOH generation experiment.

3 Prospects

As we stated in the Introduction, this laser system will be applied to generate an intense APT whose 'train envelope' duration should be shorter than 10 fs. Therefore, the following modifications of the laser system are required: (i) the compressor must be placed in a vacuum chamber to eliminate the nonlinear effect caused by air or an input glass window for an HOH generation chamber. (ii) A beam line for a loosely focused geometry [19, 20, 23] using a concave mirror should also be put in a vacuum chamber.

We have carried out a preliminary test of the loose focusing of the compressed pulse in air. After the attenuation of the energy of the compressed pulse by passing through a

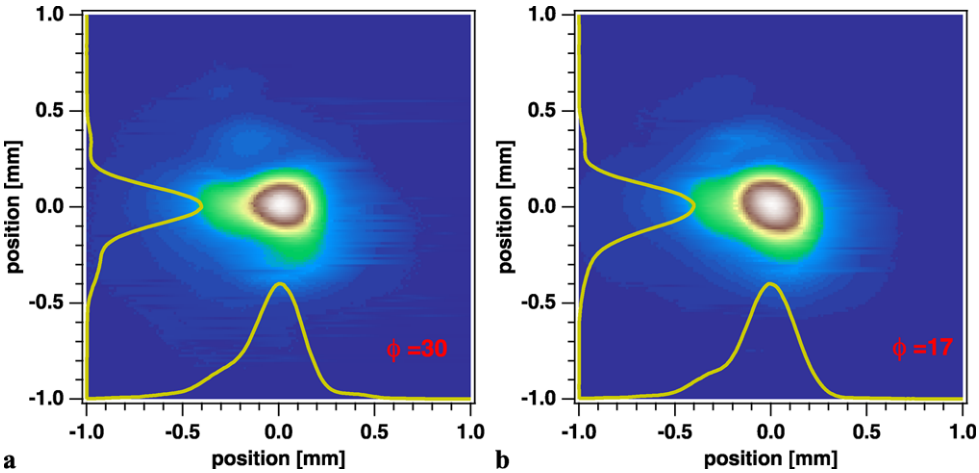

Fig. 12 Spatial profiles of loosely focused beam of compressed pulse. The iris diameters used are 30 mm (**a**) and 17 mm (**b**), respectively. The area profiles along the horizontal and vertical directions are also shown as *yellow solid curves*

high reflector mirror, the pulse is sent to a concave mirror with a radius of curvature of 9 m (4.5 m focal length). An iris with a maximum diameter of 30 mm is placed behind the concave mirror to adjust the f-number. We have observed the spatial profile of the pulse at the focal point of the concave mirror, as shown in Figs. 12(a) and (b). Although the profile in each figure cannot be perfectly fit to the Gaussian profile, it sufficiently concentrates the energy in a central spot. The ratio of the energy contained in the area within the half intensity against the energy in the whole area is 31% for Fig. 12(a) or 37% for Fig. 12(b), which is not so far from the ideal ratio of 50% for the Gaussian beam profile. Thus, we expect an efficient and intense APT generation as a Fourier synthesis of HOH fields from this multi-TW, 12-fs, 100-Hz laser system.

Acknowledgements We thank Dr. E.J. Takahashi in RIKEN for his helpful discussions concerning with HOH generation from this laser system. This work was carried out as part of Advanced Photon Science Alliance project commissioned by the Ministry of Education, Culture, Sports, Science and Technology. Y.N. gratefully acknowledges the financial support received from a grant for Scientific Research (A) 21244066. A.A.E. acknowledges the support from Junior Research Associate Program RIKEN. K.M. directed the research on laser development with a grant for the Extreme Photonics Research Group in RIKEN.

Open Access This article is distributed under the terms of the Creative Commons Attribution Noncommercial License which permits any noncommercial use, distribution, and reproduction in any medium, provided the original author(s) and source are credited.

References

1. M. Hentschel, R. Kienberger, C. Spielmann, G.A. Reider, N. Milosevic, T. Brabec, P. Corkum, U. Heinzmann, M. Drescher, F. Krausz, Nature **414**, 509 (2001)
2. E. Goulielmakis, M. Uiberacker, R. Kienberger, A. Baltuška, V. Yakovlev, A. Scrinzi, T. Westerwalbesloh, U. Kleineberg, U. Heinzmann, M. Drescher, F. Krausz, Science **305**, 1267 (2004)
3. T. Sekikawa, A. Kosuge, T. Kanai, S. Watanabe, Nature **432**, 605 (2004)
4. A. Kosuge, T. Sekikawa, X. Zhou, T. Kanai, S. Adachi, S. Watanabe, Phys. Rev. Lett. **97**, 263901 (2006)
5. G. Sansone, E. Benedetti, F. Calegari, C. Vozzi, L. Avaldi, R. Flammini, L. Poletto, P. Villoresi, C. Altucci, R. Velotta, S. Stagira, S.D. Silvestri, M. Nisoli, Science **314**, 443 (2006)
6. E. Goulielmakis, M. Schultze, M. Hofstetter, V.S. Yakovlev, J. Gagnon, M. Uiberacker, A.L. Aquila, E.M. Gullikson, D.T. Attwood, R. Kienberger, F. Krausz, U. Kleineberg, Science **320**, 1614 (2008)
7. P.B. Corkum, F. Krausz, Nature Phys. **3**, 381 (2007)
8. M. Uiberacker, T. Uphues, M. Schultze, A.J. Verhoef, V. Yakovlev, M.F. Kling, J. Rauschenberger, N.M. Kabachnik, H. Schröder, M. Lezius, K.L. Kompa, H.-G. Muller, M.J.J. Vrakking, S. Hendel, U. Kleineberg, U. Heinzmann, M. Drescher, F. Krausz, Nature **446**, 627 (2007)
9. A.L. Cavalieri, N. Müller, T. Uphues, V.S. Yakovlev, A. Baltuška, B. Horvath, B. Schmidt, L. Blümel, R. Holzwarth, S. Hendel, M. Drescher, U. Kleineberg, P.M. Echenique, R. Kienberger, F. Krausz, U. Heinzmann, Nature **449**, 1029 (2007)
10. F. Kelkensberg, C. Lefebvre, W. Siu, O. Ghafur, T.T. Nguyen-Dang, O. Atabek, A. Keller, V. Serov, P. Johnsson, M. Swoboda, T. Remetter, A. L'Huillier, S. Zherebtsov, G. Sansone, E. Benedetti, F. Ferrari, M. Nisoli, F. L'epine, M.F. Kling, M.J.J. Vrakking, Phys. Rev. Lett. **103**, 123005 (2009)
11. G. Sansone, F. Kelkensberg, J.F. Pérez-Torres, F. Morales, M.F. Kling, W. Siu, O. Ghafur, P. Johnsson, M. Swoboda, E. Benedetti, F. Ferrari, F. Lépine, J.L. Sanz-Vicario, S. Zherebtsov, I. Znakovskaya, A. L'Huillier, M.Y. Ivanov, M. Nisoli, F. Martín, M.J.J. Vrakking, Nature **465**, 763 (2010)
12. A. Baltuška, T. Udem, M. Uiberacker, M. Hentschel, E. Goulielmakis, C. Gohle, R. Holzwarth, V.S. Yakovlev, A. Scrinzi, T.W. Hänsch, F. Krausz, Nature **421**, 611 (2003)
13. M. Nisoli, S.D. Silvestri, O. Svelto, Appl. Phys. Lett. **68**, 2793 (1996)
14. P. Antoine, A. L'Huillier, M. Lewenstein, Phys. Rev. Lett. **77**, 1234 (1996)
15. Y. Mairesse, A. de Bohan, L.J. Frasinski, H. Merdji, L.C. Dinu, P. Monchicourt, P. Breger, M. Kovacev, R. Taïev, B. Carré, H.G. Muller, P. Agostini, P. Salières, Science **302**, 1540 (2003)
16. L.C. Dinu, H.G. Muller, S. Kazamias, G. Mullot, F. Augé, P. Balcou, P.M. Paul, M. Kovacev, P. Breger, P. Agostini, Phys. Rev. Lett. **91**, 063901 (2003)
17. R. López-Martens, K. Varjú, P. Johnsson, J. Mauritsson, Y. Mairesse, P. Salières, M.B. Gaarde, K.J. Schafer, A. Persson, S.

Svanberg, C.-G. Wahlström, A. L'Huillier, Phys. Rev. Lett. **94**, 033001 (2005)
18. D. Strickland, G. Mourou, Opt. Commun. **56**, 219 (1985)
19. E.J. Takahashi, Y. Nabekawa, K. Midorikawa, Opt. Lett. **27**, 1920 (2002)
20. E.J. Takahashi, Y. Nabekawa, H. Mashiko, H. Hasegawa, A. Suda, K. Midorikawa, Quantum Electron. **10**, 1315 (2004)
21. Y. Nabekawa, H. Hasegawa, E.J. Takahashi, K. Midorikawa, Phys. Rev. Lett. **94**, 043001 (2005)
22. H. Hasegawa, E.J. Takahashi, Y. Nabekawa, K.L. Ishikawa, K. Midorikawa, Phys. Rev. A **71**, 023407 (2005)
23. E. Takahashi, Y. Nabekawa, T. Otsuka, M. Obara, K. Midorikawa, Phys. Rev. A **66**, 021802 (2002)
24. K. Furusawa, T. Okino, T. Shimizu, H.H.Y. Nabekawa, K. Yamanouchi, K. Midorikawa, Appl. Phys. B **83**, 203 (2006)
25. T. Okino, K. Yamanouchi, T. Shimizu, K. Furusawa, H. Hasegawa, Y. Nabekawa, K. Midorikawa, Chem. Phys. Lett. **432**, 68 (2006)
26. Y. Nabekawa, T. Shimizu, T. Okino, K. Furusawa, H. Hasegawa, K. Yamonouchi, K. Midorikawa, Phys. Rev. Lett. **96**, 083901 (2006)
27. Y. Nabekawa, T. Shimizu, T. Okino, K. Furusawa, H. Hasegawa, K. Yamanouchi, K. Midorikawa, Phys. Rev. Lett. **97**, 153904 (2006)
28. T. Shimizu, T. Okino, K. Furusawa, H. Hasegawa, Y. Nabekawa, K. Yamanouchi, K. Midorikawa, Phys. Rev. A **75**, 033817 (2007)
29. T. Okino, K. Yamanouchi, T. Shimizu, R. Ma, Y. Nabekawa, K. Midorikawa, J. Chem. Phys. **129**, 161103 (2008)
30. Y. Nabekawa, K. Midorikawa, New J. Phys. **10**, 025034 (2008)
31. Y. Nabekawa, T. Shimizu, Y. Furukawa, E.J. Takahashi, K. Midorikawa, Phys. Rev. Lett. **102**, 213904 (2009)
32. A. Dubeitis, G. Jonasauskas, A. Piskarskas, Opt. Commun. **88**, 437 (1992)
33. S. Witte, R.T. Zinkstok, A.L. Wolf, W. Hogervorst, W. Ubachs, K.S.E. Eikema, Opt. Express **14**, 8168 (2006)
34. D. Herrmann, L. Veisz, R. Tautz, F. Tavella, K. Schmid, V. Pervak, F. Krausz, Opt. Lett. **34**, 2459 (2009)
35. G. Cheriaux, P. Rousseau, F. Salin, J.P. Chambaret, B. Walker, L.F. Dimauro, Opt. Lett. **21**, 414 (1996)
36. A.M. Weiner, Rev. Sci. Instrum. **71**, 1929 (2000)
37. M.M. Wefers, K.A. Nelson, J. Opt. Soc. Am. B **12**, 1343 (1995)
38. Y. Nabekawa, T. Togashi, T. Sekikawa, S. Watanabe, S. Konno, T. Kojima, S. Fujikawa, K. Yasui, Appl. Phys. B, suppl. **70**, S171 (2000)
39. S. Backus, C.G. Durfee III, G. Mourou, H.C. Kapteyn, M.M. Murnane, Opt. Lett. **22**, 1256 (1997)
40. F. Salin, C.L. Blanc, J. Squier, C. Barty, Opt. Lett. **23**, 718 (1998)
41. Y. Nabekawa, Y. Kuramoto, T. Togashi, T. Sekikawa, S. Watanabe, Opt. Lett. **23**, 1384 (1998)
42. Y. Nabekawa, T. Togashi, T. Sekikawa, S. Watanabe, S. Konno, T. Kojima, S. Fujikawa, K. Yasui, Opt. Express **5**, 318 (1999)
43. S. Ito, H. Nagaoka, T. Miura, K. Kobayashi, A. Endo, K. Torizuka, Appl. Phys. B **74**, 343 (2002)
44. S. Ito, H. Ishikawa, T. Miura, K. Takasago, A. Endo, K. Torizuka, Appl. Phys. B **76**, 497 (2003)
45. A.A. Eilanlou, Y. Nabekawa, K.L. Ishikawa, H. Takahashi, K. Midorikawa, Opt. Express **16**, 13431 (2008)
46. C.P.J. Barty, G. Korn, F. Raksi, C. Rose-Petruck, J. Squier, A.-C. Tien, K.R. Wilson, V.V. Yakovlev, K. Yamakawa, Opt. Lett. **21**, 219 (1996)
47. K. Yamakawa, M. Aoyama, S. Matsuoka, H. Takuma, C.P.J. Barty, D. Fittinghoff, Opt. Lett. **23**, 525 (1998)
48. Y. Nabekawa, Y. Shimizu, K. Midorikawa, Opt. Lett. **27**, 1265 (2002)
49. T. Oksenhendler, D. Kaplan, P. Tournois, G.M. Greetham, F. Estable, in *Proceedings of Conference on Lasers and Electro-Optics, 2006 and 2006 Quantum Electronics and Laser Science Conference* (Optical Society of America, Washington, 2006), p. CTuBB7
50. L. Antonucci, J. Rousseau, A. Jullien, B. Mercier, V. Laude, G. Cheriaux, Opt. Commun. **282**, 1374 (2009)
51. H. Takada, M. Kakehata, K. Torizuka, Jpn. J. Appl. Phys. **43**, L1485 (2004)
52. H. Takada, M. Kakehata, K. Torizuka, Opt. Lett. **31**, 1145 (2006)
53. P.F. Moulton, J. Opt. Soc. Am. B **3**, 125 (1986)
54. J.A. Dobrowolski, R.A. Kemp, Appl. Opt. **29**, 2876 (1990)
55. H. Takada, M. Kakehata, K. Torizuka, Jpn. J. Appl. Phys. **42**, L760 (2003)
56. H. Takada, M. Kakehata, K. Torizuka, Appl. Phys. B, suppl. **70**, S189 (2000)
57. E.J. Takahashi, H. Hasegawa, Y. Nabekawa, K. Midorikawa, Opt. Lett. **29**, 507 (2004)
58. C. Iaconis, I.A. Walmsley, IEEE J. Quantum Electron. **35**, 501 (1999)
59. V. Bagnoud, F. Salin, J. Opt. Soc. Am. B **16**, 188 (1999)